

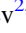


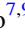







# Carbonyl Sulfide (OCS): Detections in Comets C/2002 T7 (LINEAR), C/2015 ER61 (PanSTARRS), and 21P/Giacobini–Zinner and Stringent Upper Limits in 46P/Wirtanen

Mohammad Saki<sup>1,9</sup> , Erika L. Gibb<sup>1,2,9</sup> , Boncho P. Bonev<sup>2,3,9</sup> , Nathan X. Roth<sup>4,5,9</sup> , Michael A. DiSanti<sup>2,6,9</sup> ,  
Neil Dello Russo<sup>7,9</sup> , Ronald J. Vervack, Jr.<sup>7,9</sup> , Adam J. McKay<sup>3,6,9</sup> , and Hideyo Kawakita<sup>8,9</sup> 

<sup>1</sup> Department of Physics & Astronomy, University of Missouri-St. Louis, One University Blvd., St. Louis, MO, USA; [msaki@mail.umsl.edu](mailto:msaki@mail.umsl.edu)

<sup>2</sup> Goddard Center for Astrobiology, NASA-Goddard Space Flight Center, Greenbelt, MD, USA

<sup>3</sup> Department of Physics, American University, Washington, DC, USA

<sup>4</sup> Solar System Exploration Division, Astrochemistry Laboratory Code 691, NASA-Goddard Space Flight Center, Greenbelt, MD, USA

<sup>5</sup> Universities Space Research Association, Columbia, MD, USA

<sup>6</sup> Solar System Exploration Division, Planetary System Laboratory Code 693, NASA-Goddard Space Flight Center, Greenbelt, MD, USA

<sup>7</sup> Johns Hopkins Applied Physics Laboratory, Laurel, MD, USA

<sup>8</sup> Koyoma Astronomical Observatory, Kyoto Sangyo University Motoyama, Kamingamo, Kita-ku, Kyoto 603-8555, Japan

Received 2020 March 20; revised 2020 July 1; accepted 2020 July 9; published 2020 September 25

## Abstract

Carbonyl sulfide (OCS) is one of the sulfur-bearing molecules detected in different astronomical environments, including comets. The present-day sulfur chemistry in comets may reveal much about the origin of these ices and their subsequent processing history. Cometary sulfur molecules such as H<sub>2</sub>S, H<sub>2</sub>CS, SO<sub>2</sub>, SO, CS, CS<sub>2</sub>, S<sub>2</sub>, and NS have been detected in many comets. However, OCS, the only sulfur-bearing species with fluorescence emission lines at infrared wavelengths, is under-represented in comet volatile studies, having been reported in only six comets so far. We targeted OCS with the NASA Infrared Telescope Facility in comets 46P/Wirtanen, 21P/Giacobini–Zinner, and C/2015 ER61 (PanSTARRS) in 2017–2018 using the high-resolution iSHELL spectrograph, and in C/2002 T7 (LINEAR) in 2004 using the heritage CSHELL spectrograph. In comet C/2015 ER61, the OCS abundance was similar to those measured in bright comets such as comets C/2012 S1 (ISON) and C/1996 B2 (Hyakutake), whereas in C/2002 T7 it was relatively depleted. Our OCS measurement in 21P/Giacobini–Zinner is the first definitive detection of this molecule in a Jupiter-family comet from a ground-based facility and is close to the average OCS abundance determined in comet 67P/Churyumov–Gerasimenko by the Rosetta mission. Our 3 $\sigma$  upper limit for comet 46P/Wirtanen is the lowest reported OCS abundance in any comet. We present production rates and mixing ratios (with respect to H<sub>2</sub>O) for these comets and place our results in the context of comets measured to date.

*Unified Astronomy Thesaurus concepts:* [Comet volatiles \(2162\)](#); [Near infrared astronomy \(1093\)](#); [Molecular spectroscopy \(2095\)](#); [Comets \(280\)](#)

## 1. Introduction

Comets are volatile rich small bodies that are among the most primitive remnants of the early solar system. They were some of the first bodies that formed in the protosolar nebula in the giant planet region between 5 and 30 au (or more) from the Sun. Subsequent giant planet migration ejected them into their current dynamical reservoir of either the Oort cloud (Vokrouhlický et al. 2019) or the Kuiper Belt (Nesvorný et al. 2017). As comets enter the inner solar system (heliocentric distance <3 au) increasing solar radiation causes their ices to sublime, creating a freely expanding atmosphere known as the coma, along with a dust tail and an ion tail. Most processes that may change the properties of comet nuclei only affect a thin layer (a few meters deep) from the surface, which is excavated over the course of a perihelion passage into the inner solar system (Stern 2003; Gronoff et al. 2020). Because of their small size, comets lack a known mechanism for internal self-heating; thus, it is likely that the interior compositions of comets have not been significantly modified and should reflect the composition and the conditions where (and when) they formed (Bockelée-Morvan et al. 2004; Mumma & Charnley 2011). Therefore, the chemical composition of nucleus ices should provide insights into the

initial conditions and subsequent evolution of the early solar system.

High-resolution infrared (IR) spectroscopy is a valuable way to characterize the primary volatile composition of the nucleus through analysis of fluorescent emissions in the coma. Coupled with protoplanetary disk models, the nucleus composition inferred from these studies may place observational constraints on the nascent disk mid-plane where comets formed. With about 40 comets characterized in the IR and radio and more than 200 comets cataloged at optical wavelengths, a large number of molecules have been identified in cometary atmospheres, both from ground- and space-based observations (Biver et al. 2015; Cochran et al. 2015; Le Roy et al. 2015; Dello Russo et al. 2016b; Roth et al. 2018).

Certain primary volatiles such as C<sub>2</sub>H<sub>2</sub>, CO, CH<sub>4</sub>, and OCS are under-represented in studies of comets as a whole. IR coma studies indicate that Jupiter-family comets (JFCs) (relative to Oort cloud comets; OCCs) are in general depleted in the hypervolatiles CO, CH<sub>4</sub>, and C<sub>2</sub>H<sub>6</sub>, which may reflect the effects of repeated close perihelion passages on their volatile content. On the other hand, large optical studies of product species found no correlation between dynamical family and carbon-chain depletion, suggesting that these differences may instead be primordial and indicative of differences in formation histories for JFCs compared to OCCs (Dello Russo et al. 2016b and references therein). The detection of crystalline silicates in some

<sup>9</sup> Visiting Astronomer at the Infrared Telescope Facility, which is operated by the University of Hawaii under contract NNH14CK55B with the National Aeronautics and Space Administration.

comets coupled with updates in dynamical models (e.g., Levison et al. 2011) suggests that scattering processes and large-scale mixing of materials in the early solar nebula have complicated the distinction between comet-forming regions (Bockelée-Morvan et al. 2000, 2016; Gomes et al. 2005; Zolensky et al. 2006; Dello Russo et al. 2016b). Therefore, the Oort cloud and Kuiper Belt contain comets that may represent varying (or, at the other extreme, largely overlapping) formation regions in the solar nebula. The Rosetta mission to comet 67P/Churyumov–Gerasimenko (hereafter 67P) revealed a heterogeneous nucleus, adding more complexity to these scenarios (Le Roy et al. 2015; Rickman et al. 2015) and stimulating fundamental questions concerning the extent to which abundances measured in cometary comae are representative of the pristine composition of nucleus ices (see A’Hearn 2017 for a discussion of these questions). In this work we address these complex questions by significantly increasing the number of OCS measurements in comets, thereby advancing our understanding of their sulfur chemistry. We report the detection of OCS in two OCCs, C/2015 ER61 (PanSTARRS) (hereafter ER61) and C/2002 T7 (LINEAR) (hereafter T7), and in one JFC, 21P/Giacobini–Zinner (hereafter G–Z). We also present a  $3\sigma$  upper limit for OCS in JFC 46P/Wirtanen (hereafter Wirtanen). In Section 2, we discuss the importance of OCS in comets. In Section 3, we discuss our observations and our data reduction methodology. In Section 4, we present our results. In Section 5, we discuss our results and place them in the context of comets characterized to date.

## 2. OCS in Comets

Carbonyl sulfide (OCS) is one of the parent volatiles (native ices) that has been stored for  $\sim 4.5$  billion years in icy grains in the nuclei of comets. The present-day sulfur chemistry in comets may reveal much about the origin of these ices and their subsequent processing history, making the measurement of sulfur-bearing molecules in comets an important piece to the puzzle of cometary origins (Dello Russo et al. 1998). Sulfur species should be present in cometary nuclei since comets were likely formed in the mid-plane of the protoplanetary disk from icy grains, where volatiles (including OCS) could freeze out on the surface of dust grains. OCS serves as a link between sulfur- and oxygen-bearing species. It is extremely under-represented in the current sample of measurements of cometary volatiles, and the only known sulfur-bearing species in comets with strong transitions at IR wavelengths; its  $\nu_3$  band near  $4.85 \mu\text{m}$  is inherently very strong, being an order of magnitude stronger than the CO  $\nu_1$  band near  $4.7 \mu\text{m}$  and rivaling the strength of the CO<sub>2</sub>  $\nu_3$  band that renders the region from  $\sim 4.1$  to  $4.4 \mu\text{m}$  totally opaque to ground-based observations. Our OCS measurements are well-suited to address the paucity of OCS detections in comets.

Despite being inherently strong, OCS has been detected in only six comets to date: C/1995 O1 Hale–Bopp (hereafter Hale–Bopp), C/1996 B2 Hyakutake (hereafter Hyakutake), 67P (via the Rosetta mission), C/2012 S1 (ISON), C/2014 Q2 (Lovejoy), and 2P/Encke (tentative); see Section 5 for more details. The small number of OCS measurements is largely due to limitations in spectral coverage and/or sensitivity in previously available instruments. Owing to its piecewise continuous nature, targeting OCS with NIRSPEC at Keck requires a second  $M$ -band setting in addition to the standard one used to measure H<sub>2</sub>O

together with the strongest CO lines seen in comets (e.g., see Gibb et al. 2012), while the limited sensitivity and small spectral grasp of the previous facility spectrograph at the Infrared Telescope Facility (IRTF) (CSHELL; Tokunaga et al. 1990; Greene et al. 1993) limited measuring OCS to bright comets. With iSHELL, the OCS  $\nu_3$  band is fully encompassed together with H<sub>2</sub>O and CO within a single instrument setting (see Section 3) and, unlike NIRSPEC or CSHELL, active guiding is feasible at wavelengths independent of the bandpass used to obtain spectra (specifically, for the observations of C/2015 ER61, 21P, and 46P included in this study, the iSHELL M2 setting; see Section 3).

## 3. Observations and Data Reduction

We targeted OCS in comets Wirtanen, G–Z, and ER61 in 2017–2018 using the high-resolution ( $\lambda/\Delta\lambda \sim 40,000$ ) IR immersion grating echelle spectrograph iSHELL (Rayner et al. 2012, 2016) at the 3 m NASA IRTF on Maunakea, HI. The superior IR active guiding capabilities of iSHELL enabled us to achieve observing efficiency of up to 80%. This paper reports results from two iSHELL settings: our custom  $L$ -band setting (“Lcustom,” covering  $\sim 2.8$ – $3.2 \mu\text{m}$ ) which contains multiple strong transitions of H<sub>2</sub>O, sampling a range of excitation energies and enabling robust determination of rotational temperature ( $T_{\text{rot}}$ ), and M2 (covering  $\sim 4.5$ – $5.2 \mu\text{m}$ ) which samples emissions of OCS and H<sub>2</sub>O simultaneously. The iSHELL observations were performed with a  $0''.75$  wide (6 pixel wide) slit, oriented along the projected Sun–comet line on all dates.

We also present archival data of comet T7 acquired in 2004 using CSHELL at resolving power  $\lambda/\Delta\lambda \sim 25,000$  using the  $1''.0$  (5 pixel) wide slit. T7 was a daytime object, which precluded use of the optical guide camera in CSHELL. Instead, images of the comet were taken before and after each sequence of scans to monitor and correct for cometary drift. To correct slight errors in tracking and re-position the comet on the array, the CSHELL slit was set at its default position angle of  $270^\circ$  (east–west on the sky).

To achieve flux calibration, a suitably bright IR flux standard star was observed using a  $4''$  wide slit on each date and for each setting (using a wider slit for the star than was used for the comet helps minimize loss of signal and thereby achieves a truer measure of the stellar continuum; see Bonev 2005; Radeva et al. 2010; Villanueva et al. 2011 for further details regarding flux calibrations). Table 1 shows the observing log for the data presented in this paper.

All observations were performed using a standard ABBA nod pattern (sequence of four scans) where the A and B beams were placed symmetrically about the midpoint along the  $15''$  (for iSHELL) or  $30''$  (for CSHELL) longslit and separated by half its length. Thus, the comet was present in both beams, thereby providing an increased signal-to-noise ratio ( $S/N$ ) (by a factor of up to  $\sqrt{2}$  compared with nodding to blank sky). Combining the frames as A–B–B+A (comet–sky–sky+comet) canceled out background thermal continuum, sky emission (lines and continuum), and instrumental biases to second order in airmass (see Figure 2 of DiSanti et al. 2001). The data were then dark-subtracted (to account for high dark-current pixels), flat-fielded (using an internal continuum lamp), cleaned of cosmic ray hits and hot pixels, and rectified to produce two-dimensional (spatial-spectral) frames, where each row corresponds to a constant (and unique) spatial position along the slit,

**Table 1**  
OCS Observation Log

Comet	UT Date	Instrument	Time (UT)	$R_h$ (au)	$dR_h/dt$ (km s <sup>-1</sup> )	$\Delta$ (au)	$d\Delta/dt$ (km s <sup>-1</sup> )	$T_{\text{int}}$ (minutes)
T7 <sup>a</sup>	2004 May 5	CSHELL	15:52–21:14	0.671	15.27	0.631	−65.67	16
	2004 May 9	CSHELL	15:44–21:05	0.713	18.54	0.484	−61.37	12
ER61 <sup>b</sup>	2017 May 12	iSHELL	14:16–17:16	1.043	1.27	1.251	9.25	94
G–Z <sup>c</sup>	2018 Jul 25	iSHELL	12:02–13:58	1.20	−12.72	0.64	−13.66	85
	2018 Jul 28	iSHELL	13:32–15:44	1.18	−12.23	0.61	−13.39	96
	2018 Jul 29	iSHELL	13:25–15:23	1.17	−12.05	0.61	−13.31	86
Wirtanen <sup>d</sup>	2018 Dec 14	iSHELL	09:06–11:59	1.055	0.45	0.078	−1.49	122
	2018 Dec 19	iSHELL	05:39–08:03	1.058	1.91	0.079	2.00	114

**Notes.**  $R_h$ ,  $dR_h/dt$ ,  $\Delta$ ,  $d\Delta/dt$ , and  $T_{\text{int}}$  are heliocentric distance, heliocentric velocity, geocentric distance, geocentric velocity, and total on source integration time, respectively. For comets observed with iSHELL, the slit position angle (PA) was oriented along the projected Sun–comet line on all dates.

<sup>a</sup> T7 reached perihelion (0.614 au) on 2004 April 23 and was closest to Earth (0.266 au) on 2004 May 19. We targeted OCS on two dates, May 5 and 9.

<sup>b</sup> ER61 reached perihelion (1.042 au) on 2017 May 10 and was closest to Earth (1.178 au) on 2017 April 18, shortly after its outburst on April 4 (M. Saki et al., in preparation). We observed ER61 and targeted the OCS spectral region on 2017 May 12.

<sup>c</sup> G–Z reached perihelion (1.010 au) on 2018 September 10 and was closest to Earth (0.077 au) on the same day.

<sup>d</sup> Wirtanen reached perihelion (1.055 au) on 2018 December 12 and was closest to Earth (0.077 au) on 2018 December 16. We targeted the OCS spectral region on December 14 and 19.

and each column to a unique wavelength. We found that spatially resampling using a third-order polynomial more completely removed the curvature in the spatial dimension from iSHELL frames and so employed this in place of previously used second-order polynomials (DiSanti et al. 2017; Roth et al. 2018). The spectral frames were spatially registered and spectra were then extracted by summing signal over 15 rows (approximately  $2''/5$ ), seven rows to each side of the nucleus, defined as the peak of dust emission in a given spectral order. Our observational procedures and data reduction algorithms have been rigorously tested and well documented in peer-reviewed literature (Dello Russo et al. 1998; DiSanti et al. 2001, 2006, 2014, 2017; Bonev 2005; Villanueva et al. 2009; Radeva et al. 2010).

The Planetary Spectrum Generator (Villanueva et al. 2018) was used to generate atmospheric models, to assign a wavelength scale to the spectra, and to establish absolute column burdens of the component-absorbing species in the terrestrial atmosphere. We convolved the fully resolved atmospheric transmittance function to the resolving power of the data and scaled it to the level of the comet continuum. We then subtracted the modeled continuum to isolate cometary emission lines as previously described (e.g., DiSanti et al. 2016). The procedure is illustrated in Figure 1. Synthetic models of fluorescent emission for our targeted species were compared to observed line intensities, after correcting each modeled line intensity for the monochromatic atmospheric transmittance at its Doppler-shifted wavelength (according to the geocentric velocity of the comet at the time of the observation). The g-factors used in synthetic fluorescent emission models in this study were generated with quantum mechanical models for OCS, CN (Paganini & Mumma 2016), and H<sub>2</sub>O (Villanueva et al. 2012).

#### 4. Results

We determined water rotational temperatures ( $T_{\text{rot}}$ ), OCS and H<sub>2</sub>O production rates ( $Q_s$ ), and the abundance (or “mixing”) ratio  $Q_{\text{OCS}}/Q_{\text{H}_2\text{O}}$  (expressed in %) for all comets in this paper. We found consistent results and excellent fits to the comet

spectra (both for telluric absorptions and for cometary emission features).

##### 4.1. Spatial Profile as Diagnostic for OCS Outgassing Source

In comet T7 the OCS emissions were sufficiently strong when coadded on both dates (May 5 and 9) to determine the spatial profile along the slit (see Figure 2). The H<sub>2</sub>O production rate and the relative OCS abundances were consistent on both dates, thus we coadded the lines for both molecules to increase the S/N. Figure 2 suggests that the spatial distribution of OCS in T7 followed that of H<sub>2</sub>O as well as the dust within measurement uncertainties. Owing to limited S/N along the slit, we were unable to extract meaningful emission spatial profiles for OCS in the other comets presented here. Most high-resolution IR observations of comets permit investigations of processes in the inner coma, where both nucleus and extended sources (i.e., release from one or more sources in the coma) may contribute to the production and spatial distribution of a particular volatile. Analysis of spatial profiles for coma molecules can indicate whether their distribution differs from that expected for direct sublimation from the nucleus, as opposed to release from extended sources in the coma (Dello Russo et al. 1998, 2016a; DiSanti et al. 2001; Brooke et al. 2003). The spatial profile for molecules produced by direct sublimation peak in intensity at (or at least near) the position of the nucleus before falling off with increasing nucleocentric distance ( $\rho$ ) as  $\rho^{-1}$ , whereas molecules having an extended source display a flatter distribution, falling off more slowly with  $\rho$  (e.g., see Figure 3 in Dello Russo et al. 1998). In our OCS study, the OCS spatial distribution is formally consistent with H<sub>2</sub>O; however, the low S/N does not allow for a definitive conclusion on the presence (or absence) of a distributed OCS source in the coma of comet T7 (see Figure 2), but the spatial profiles of H<sub>2</sub>O and OCS are consistent with common outgassing sources seen in other comets (e.g., Hale–Bopp, ISON). Evidence for the existence of OCS extended sources has been identified in the bright comets Hale–Bopp near  $R_h = 1$  au, and in ISON at  $R_h = 0.46$  au. In comet Hale–Bopp near perihelion, the long-slit IR observations suggested OCS originated substantially or even predominantly

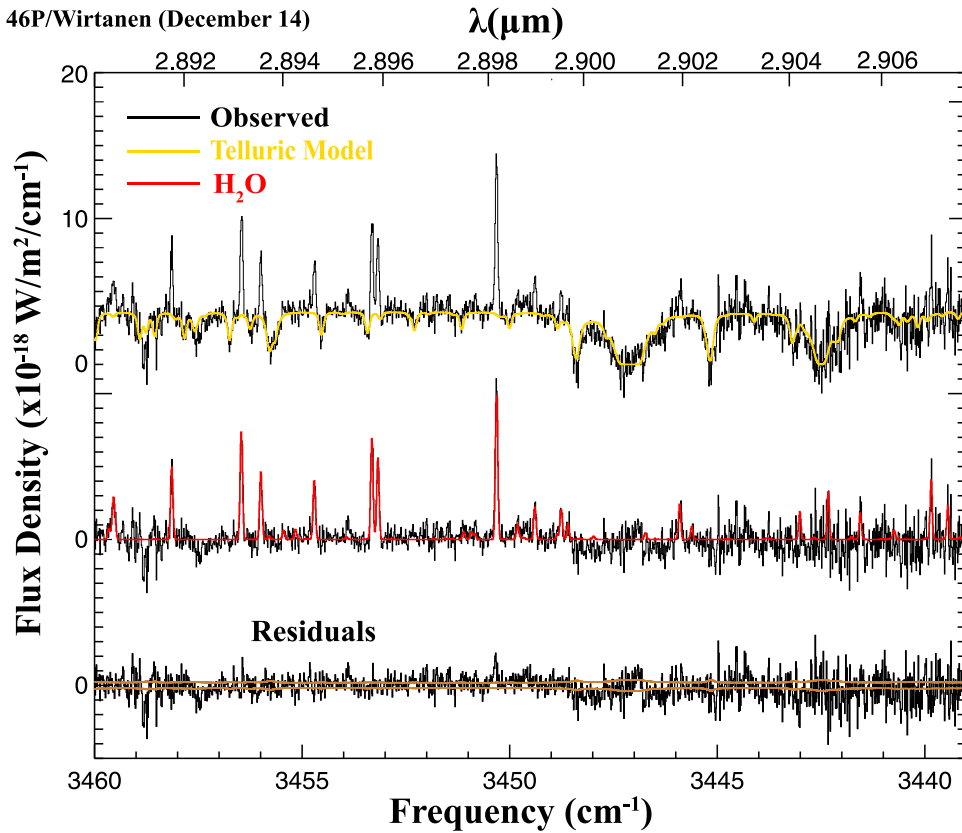


**Figure 1.** Extracted spectra showing clear detections of H<sub>2</sub>O in comet Wirtanen, superimposed on the cometary continuum on UT 2018 December 14. The yellow trace overplotted on the uppermost cometary spectrum is the best-fit telluric transmittance model (convolved to the instrumental resolution). Directly below is the residual spectrum (after subtracting the telluric absorption model), with the H<sub>2</sub>O fluorescence emission model overplotted in red. At the bottom of the panel is the residual spectrum (after subtracting the telluric absorption model and H<sub>2</sub>O fluorescence model), with the  $1\sigma$  uncertainty envelope overplotted in bronze.

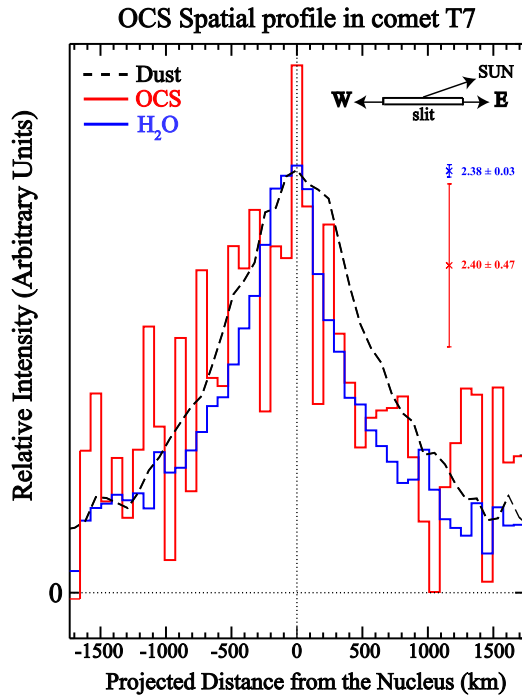


**Figure 2.** Spatial profiles of OCS (red line) simultaneously measured with dust (black dashed line) and H<sub>2</sub>O (blue line) in comet T7 on UT 2004 May 5 and 9 combined. The slit was oriented in its default position (east–west) with the Sun-facing direction to the right as indicated. The combined growth factor and its  $\pm 1\sigma$  uncertainty measured from each profile are indicated at the right.

from extended sources ( $\sim 70\%$ ; see Dello Russo et al. 1998 for further details). The broad and flat spatial distribution of OCS in comet ISON also suggested that a significant fraction may have come from an extended source (Dello Russo et al. 2016a).

#### 4.2. Rotational Temperature

Rotational temperatures ( $T_{\text{rot}}$ ) were determined using correlation and excitation analyses that have been extensively described in the literature (e.g., Bonev 2005; DiSanti et al. 2006; Bonev et al. 2008; Villanueva et al. 2008). In general, well-constrained rotational temperatures can be determined for individual species with intrinsically bright lines and for which a sufficiently broad range of excitation energies is sampled. These conditions were met for strong H<sub>2</sub>O lines centered near  $3452 \text{ cm}^{-1}$  in CSHELL spectra, and in Lcustom order 179 with iSHELL spanning  $\sim 3437.8\text{--}3465.8 \text{ cm}^{-1}$ , and were augmented by including H<sub>2</sub>O lines in additional iSHELL orders (see Figure 1 and Table 2).

For T7 the  $T_{\text{rot}}$  for H<sub>2</sub>O on May 5 ( $104^{+6}_{-10}$  K) was consistent with that from May 9 ( $106^{+4}_{-5}$  K). The H<sub>2</sub>O rotational temperature for ER61 was measured as  $60^{+6}_{-5}$  K on May 12. For our G–Z analysis, we calculated production rates and mixing ratios at  $T_{\text{rot}} = 48$  and  $64$  K, consistent with rotational temperatures derived from CO ( $64^{+15}_{-11}$  K) and H<sub>2</sub>O ( $48^{+19}_{-13}$  K) on July 28 and 29, respectively (Roth et al. 2020). We used three iSHELL settings for Wirtanen on December 14 and 19, and were able to retrieve well-constrained rotational temperatures on both dates. We found the  $T_{\text{rot}}$  for H<sub>2</sub>O as measured from the



**Table 2**  
OCS Abundances

Molecules	$T_{\text{rot}}(k)$	Growth Factor	$Q$ (molecules $s^{-1}$ )	Abundance (%)
Wirtanen 2018 Dec 14				
H <sub>2</sub> O	$84 \pm 3$	$2.32 \pm 0.08$	$(5.95 \pm 0.23) \times 10^{27}$	100
OCS	(84)	(2.32)	$<9.38 \times 10^{23}$	$<0.016^a$
Wirtanen 2018 Dec 19				
H <sub>2</sub> O	$86_{-14}^{+17}$	$1.98 \pm 0.08$	$(6.04 \pm 0.3) \times 10^{27}$	100
OCS	(86)	(1.98)	$<9.92 \times 10^{23}$	$<0.016^a$
G–Z Jul 25, 28, and 29 (combined)				
H <sub>2</sub> O	(48) <sup>b</sup>	$1.90 \pm 0.04^c$	$(2.63 \pm 0.20) \times 10^{28}$	100
OCS	(48)	(1.9)	$(307 \pm 0.41) \times 10^{25}$	$0.116 \pm 0.022$
H <sub>2</sub> O	(64) <sup>b</sup>	$1.90 \pm 0.04^c$	$(2.86 \pm 0.22) \times 10^{28}$	100
OCS	(64)	(1.9)	$(3.10 \pm 0.46) \times 10^{25}$	$0.108 \pm 0.021$
ER61 2017 May 12				
H <sub>2</sub> O	$60_{-5}^{+6}$	$2.34 \pm 0.36$	$(7.04 \pm 0.25) \times 10^{28}$	100
OCS	(60)	(2.34)	$(1.06 \pm 0.19) \times 10^{26}$	$0.15 \pm 0.031$
T7 2004 May 5				
H <sub>2</sub> O	$104_{-10}^{+6}$	$2.34 \pm 0.03$	$(5.39 \pm 0.25) \times 10^{29}$	100
OCS	(104)	(2.34)	$(1.95 \pm 0.47) \times 10^{26}$	$0.036 \pm 0.009$
T7 2004 May 9				
H <sub>2</sub> O	$106_{-5}^{+4}$	$2.51 \pm 0.05$	$(5.08 \pm 0.16) \times 10^{29}$	100
OCS	(106)	(2.51)	$(2.22 \pm 0.21) \times 10^{26}$	$0.043 \pm 0.006$

**Notes.** Values in parenthesis are assumed.

<sup>a</sup>  $3\sigma$  upper limit.

<sup>b</sup> Temperature from Roth et al. (2020).

<sup>c</sup> The average of the growth factors (from Roth et al. 2020).

Lcustom setting ( $84 \pm 3$  K) on December 14 was in agreement with that from the M2 setting ( $83 \pm 7$  K), thus we used  $T_{\text{rot}} = 84$  K when determining production rates and mixing ratios. The H<sub>2</sub>O  $T_{\text{rot}}$  on December 19 was also consistent with that on December 14 ( $86_{-11}^{+17}$  K). We were unable to measure rotational temperatures for OCS in any of the observations reported here, so we adopted the rotational temperature of simultaneously measured H<sub>2</sub>O within the same setting (M2). Rotational temperatures for different molecules within the same comet and the same instrumental setting are generally found to be consistent even for molecules with different photodissociation lifetimes (e.g., see DiSanti et al. 2006, 2016; Anderson 2010; Gibb et al. 2012, supporting this approach).

### 4.3. Production Rates and Mixing Ratios

Production rates for sampled species were determined using the appropriate fluorescence model at the measured (or assumed) rotational temperature. Nucleus-centered production rates ( $Q_{\text{NC}}$ , molecules  $s^{-1}$ ) were calculated using the well-established formalism relating line flux, fluorescence g-factor, and physical (gas outflow speed, photodissociation lifetime) and geometric parameters ( $R_h$ ,  $\Delta$ ; see Dello Russo et al. 1998; DiSanti et al. 2001, 2006, 2014; Bonev 2005; Villanueva et al. 2011).  $Q_{\text{NC}}$  is then scaled by a growth factor (GF), which relates molecular production rates in the fraction of the coma along the column described by the beam (of size  $0''.75 \times 2''.5$  for iSHELL, and  $1'' \times 3''$  for CSHELL) to the global

production rate ( $Q_{\text{global}}$ ). This method analyzes spatial profiles of emission using the ‘‘Q-curve’’ formalism, dating back to the analysis of OCS in comet Hale–Bopp (Dello Russo et al. 1998). A canonical spherically symmetric outflow velocity,  $v_{\text{gas}} = 800 R_h^{-0.5} \text{m s}^{-1}$ , was assumed in determining our production rates. This velocity is based on velocity-resolved observations of several moderately bright comets at radio wavelengths (Biver et al. 2006; Cordiner et al. 2014; also see Bonev 2005, supporting this assumption). We were able to explicitly determine that OCS traced the spatial profile of H<sub>2</sub>O in comet T7 and the derived OCS GF (combined on both dates) was consistent with the GF derived for H<sub>2</sub>O (see Figure 2); therefore, we assumed the GF of simultaneously measured H<sub>2</sub>O when calculating OCS production rates ( $Q$ s). Global production rates for all the comets targeted in this paper along with OCS mixing ratios relative to water are presented in Table 2.

For comet T7 we measured OCS mixing ratios of  $0.036\% \pm 0.009\%$  and  $0.043\% \pm 0.006\%$  on May 5 and May 9 respectively. Figures 3(A), (B) show extracted spectra with clear OCS, CN, and H<sub>2</sub>O emissions in T7 (with traces and labels as described in Figure 1). In ER61, the OCS mixing ratio was found to be  $0.150\% \pm 0.031\%$ . Figure 3(C) shows detections of H<sub>2</sub>O, CN, and OCS lines in ER61 on May 12. In the case of G–Z, since the H<sub>2</sub>O production rate and relative OCS abundances were consistent throughout our July observations, we coadded the spectra on all three dates (July 25, 28, and 29), and found OCS mixing ratios of  $0.116\% \pm 0.022\%$

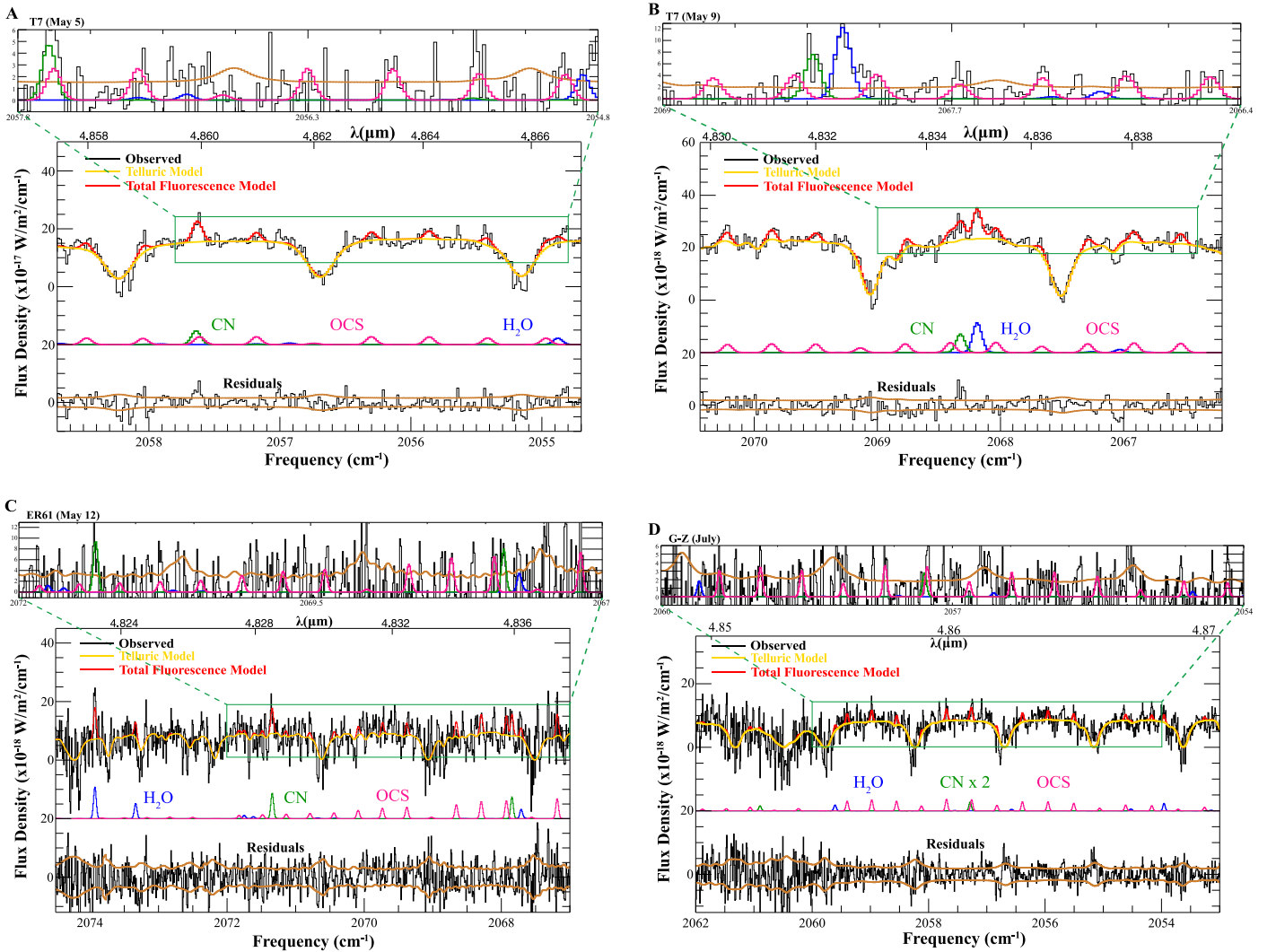


**Figure 3.** The detections of OCS are shown in comet T7 (A and B), ER61 (C), and G–Z (D). The zoomed subplot highlights the location and intensity of OCS emission lines with respect to  $1\sigma$  uncertainty envelope plotted in bronze; each subplot has the same units as the larger plot. Yellow traces overlapped on the uppermost cometary spectra are the telluric absorption models (convolved to the instrumental resolution), while the total modeled fluorescent emissions are overlapped in red. Individual fluorescent emission models (color-coded by species for clarity) are plotted below. At the bottom of each panel is the residual spectrum (after subtracting the telluric absorption model and all relevant fluorescent emission models) with the  $1\sigma$  uncertainty envelope overlapped in bronze.

(assuming  $T_{\text{rot}} = 48$  K) and  $0.108\% \pm 0.021\%$  (assuming  $T_{\text{rot}} = 64$  K), demonstrating that the abundance of OCS relative to  $\text{H}_2\text{O}$  was not sensitive to the assumed  $T_{\text{rot}}$ . Figure 3(D) shows the clear detections of OCS, CN and  $\text{H}_2\text{O}$  in G–Z. We were unable to detect any OCS emission lines with S/N greater than 5 for Wirtanen, yet our derived  $3\sigma$  upper limits on both December 14 and 19 are consistent (being  $<0.016\%$ ). Figure 1 shows the detection of  $\text{H}_2\text{O}$  in comet Wirtanen in Lcustom order 179 on December 14. For the comets analyzed here, we have excluded OCS lines that are blended with CN and/or  $\text{H}_2\text{O}$ . CN emissions in all of these comets were strong, consistent with other comets measured at similar  $R_h$  (see Dello Russo et al. 2016b for more details).

Individual OCS emission lines are not detected in all of the comets in this paper (see Figure 3); however, by combining the flux of all the unblended OCS lines we achieved a sensitive measurement of OCS production rate and its abundance relative to  $\text{H}_2\text{O}$  in comets T7, G–Z, and ER61 and report a stringent upper limit in comet Wirtanen. Centered on the Doppler-shifted line frequency, line flux was measured for a given line by integrating over the spectral range of each line in each comet.

Identical measurements were performed away from the expected line centers ( $\nu'_i = \nu_i + \Delta\nu$ ), with  $\Delta\nu$  ranging from  $-0.3$  to  $+0.3$   $\text{cm}^{-1}$ . This method has been validated for weak species in other comets measured at IR wavelengths (see Villanueva et al. 2009; Paganini et al. 2017). In the case of sampling noise, the peak flux will occur offset from the Doppler-shifted line center. Instead, the peak composite flux for each comet is found at the expected position (see Figure 4). We performed the same measurement for  $\text{H}_2\text{O}$  and found that the OCS composite line has the same shape and width as the  $\text{H}_2\text{O}$  composite line. As an example, we plotted the  $\text{H}_2\text{O}$  composite line for comet G–Z in Figure 4(A).

## 5. Discussion

### 5.1. OCS and Other Sulfur-bearing Species in Comets

Roughly 40 comets have been sampled with high-resolution IR spectroscopy and differences in composition have been noted among both OCCs and JFCs. This relatively small sample size has made the development of a chemistry-based classification system difficult. OCS is one of the under-represented molecules in comet

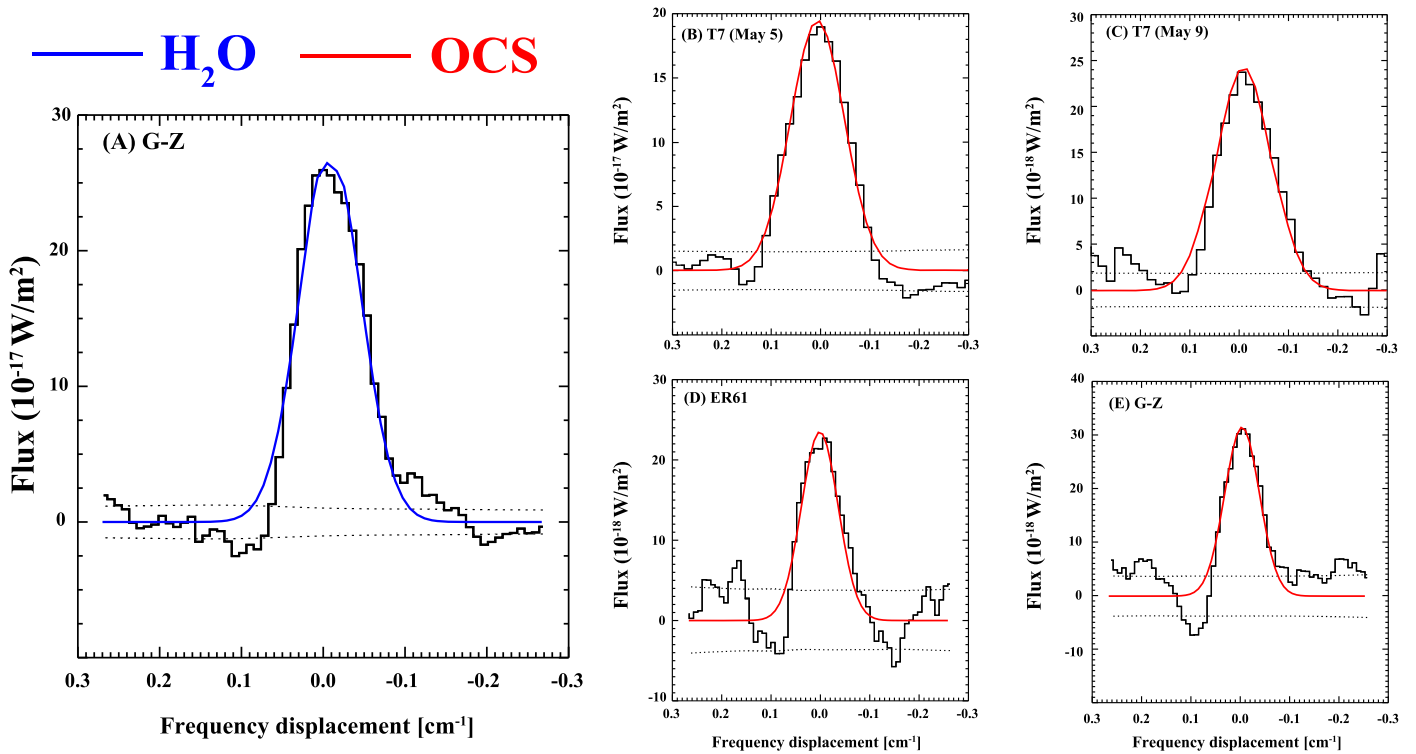


**Figure 4.** Panel A shows the H<sub>2</sub>O composite emission line in comet G–Z. (B)–(E) show the composite OCS emission line by combining unblended individual OCS lines for each comet. The 1 $\sigma$  noise envelope is shown as dotted lines. The H<sub>2</sub>O and OCS models are plotted in blue and red respectively.

studies due largely to limitations in sensitivity and lack of spectral coverage in earlier instruments (see Sections 1 and 2, and the discussion in Dello Russo et al. 2016a). However, other sulfur species (e.g., H<sub>2</sub>S, H<sub>2</sub>CS, SO<sub>2</sub>, SO, CS, CS<sub>2</sub>, S<sub>2</sub>, and NS) have been detected in many comets (see Table 5 in Le Roy et al. 2015, Table 1 in Bockelée-Morvan et al. 2004, and Table A2 in Calmonte et al. 2016 for a list of detected sulfur-bearing species and their abundances in comets).

In contrast, detections of OCS have been reported in only six comets to date (mostly OCCs). It was first detected through its radio lines at 145.947 GHz by Woodney et al. (1997) in comet Hyakutake, and confirmed by several other radio lines in comet Hale–Bopp (e.g., Bockelée-Morvan et al. 2000). Strong IR OCS lines close to 4.9  $\mu$ m were reported by Dello Russo et al. (1998) in both Hyakutake and Hale–Bopp. The Rosetta spacecraft detected OCS in comet 67P (Le Roy et al. 2015; Bockelée-Morvan et al. 2016). Additional ground-based detections have been reported for comets ISON (Dello Russo et al. 2016a), Lovejoy (Biver et al. 2015), and 2P/Encke (at 4 $\sigma$ ) (Roth et al. 2018). In this paper, we add two OCCs (comet T7 and ER61) and one JFC (G–Z) to this list (see Figure 5 and Table 2). Our OCS measurement in comet G–Z represents its first secure ground-based detection in a JFC. Abundances are given in Table 3.

Ecliptic (short-period) comets and specifically JFCs are typically depleted in certain trace volatiles relative to OCCs, perhaps due to thermal processing (Dello Russo et al. 2016b; DiSanti et al. 2017; Roth et al. 2018, 2020). The first OCS measurement for a short-period comet did not occur until 2015 via the Rosetta mission to comet 67P, for which the large orbital obliquity ( $\sim 52^\circ$ ) of its rotation axis leads to strong seasonal effects on its nucleus. Le Roy et al. (2015) searched for multiple sulfur species, including OCS, in the coma of 67P and found an

OCS abundance of 0.017% relative to H<sub>2</sub>O (similar to our 3 $\sigma$  upper limit in Wirtanen; Table 2) for summer and 0.098% (similar to our measured OCS abundance in G–Z, for  $T_{\text{rot}} = 64$  K) for the winter hemisphere (see Table 3 and Le Roy et al. 2015 for further details). Bockelée-Morvan et al. (2016) found an average OCS abundance of 0.12% relative to H<sub>2</sub>O for pre-perihelion observations (2015 July 8–August 10) and a higher average of 0.18% relative to H<sub>2</sub>O (due to outburst and high depth of ablation) for post-perihelion observations (2015 August 16–September 27). The average OCS abundance in comet 67P is similar to our measured abundance in comet G–Z. Recently, Calmonte et al. (2016) reported the detection of new sulfur-bearing species (e.g., CH<sub>3</sub>SH, C<sub>2</sub>H<sub>6</sub>S) in the coma of comet 67P.

## 5.2. Formation of OCS

OCS has been identified in a variety of astronomical environments. OCS can catalyze the coupling of amino acids and so is of particular interest for astrobiology (Leman et al. 2004). It has been observed in the atmospheres of Venus, Jupiter, and Io as well as in interstellar ice and comets (e.g., Kamp & Taylor 1990; Woodney et al. 1997; Dello Russo et al. 1998; Sakai et al. 2014; Le Roy et al. 2015). Only <0.1% of the sulfur cosmic abundance can be accounted for in gas-phase molecules (Tieftrunk et al. 1994; also see Le Gal et al. 2019 for further details), suggesting that most sulfur-bearing species are locked into icy mantles coating interstellar dust grains (Millar & Herbst 1990; Ruffle et al. 1999; Vidal et al. 2017; Laas & Caselli 2019).

Recent spectral line surveys have increased the number of known interstellar sulfur molecules (see Vastel et al. 2018 and references therein), and recent astrochemical models have improved our understanding of sulfur-bearing species in interstellar environments (e.g., Woods et al. 2015; Vidal et al. 2017;

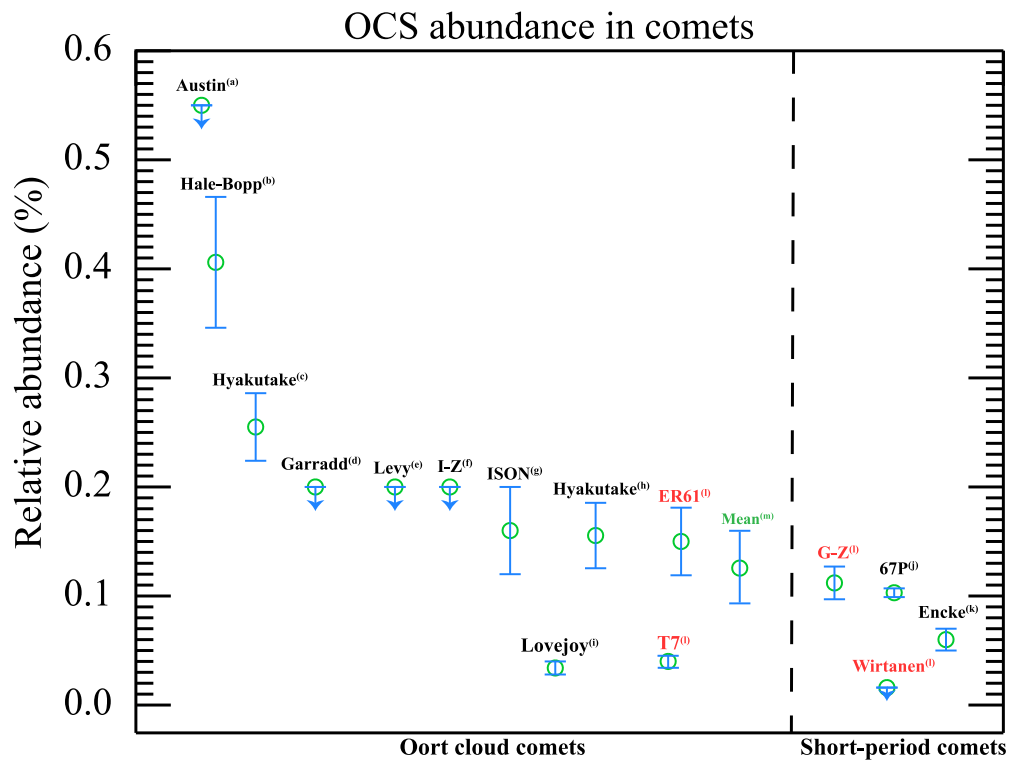


**Figure 5.** Measured OCS abundances (relative to  $\text{H}_2\text{O}$ ) in comets. (a) DiSanti et al. (1992), (b) Dello Russo et al. (1998) (IR), Bockelée-Morvan et al. (2000) (radio), (c) Dello Russo et al. (1998) (near-IR), (d) Paganini et al. (2012), (e) Bockelée-Morvan et al. (1990), (f) Bockelée-Morvan et al. (2004), (g) Dello Russo et al. (2016a), (h) Woodney et al. (1997), Biver et al. (1999), (i) Biver et al. (2015), (j) Le Roy et al. (2015), Bockelée-Morvan et al. (2016), (k) Roth et al. (2018), (l) this work, (m) OCS unweighted mean abundance among comets ( $0.126 \pm 0.034\%$ ). Note: owing to the significance of Wirtanen’s upper limit we have included half of its value when calculating the unweighted mean.

Vidal & Wakelam 2018). Laas & Caselli (2019) used a new sulfur depletion model that accurately reproduced most of the known gas-phase sulfur-bearing molecular abundances observed in interstellar clouds. Their model also predicts that most of the sulfur-bearing species are trapped on icy grains, consistent with observations. Processing of interstellar ice mixtures containing simple sulfur-bearing species yields a highly heterogeneous mixture of products similar to the chemistry that has been detected in both cometary ices and meteoritic material (see Ehrenfreund et al. 2002; Jiménez-Escobar et al. 2014; Calmonte et al. 2016 and references therein).

OCS is also one of the sulfur-bearing molecules detected in icy grain mantles toward protostars and disks (e.g., Geballe et al. 1985; Palumbo et al. 1997; Zasowski et al. 2009; Fuente et al. 2010; Guilloteau et al. 2013, 2016; Pacheco-Vázquez et al. 2016; Sakai et al. 2016; Phuong et al. 2018; Teague et al. 2018). Palumbo et al. (1997) found that OCS is embedded in  $\text{CH}_3\text{OH}$  rich ices in protostar W33A. Understanding the path that could contribute to OCS formation in these environments requires both modeling and laboratory experiments.

Extensive experimental studies have been performed analyzing the formation of OCS both in  $\text{H}_2\text{O}$ -free and  $\text{H}_2\text{O}$ -dominated ices using CO or  $\text{CO}_2$  as the C-bearing species and  $\text{H}_2\text{S}$  or  $\text{SO}_2$  as the sulfur-bearing sources (see Moore et al. 2007; Ferrante et al. 2008 and references therein). The CO abundance is relatively high in interstellar ices, and Hawkins et al. (1985) demonstrated that CO is capable of capturing S atoms to produce OCS. Experiments have also shown that  $\text{H}_2\text{S}$  can dissociate into 2H and S (Isoniemi et al. 1999). Therefore, one possible reaction sequence to produce OCS is:  $\text{H}_2\text{S} \rightarrow 2\text{H} + \text{S}$

and  $\text{S} + \text{CO} \rightarrow \text{OCS}$  (see Ferrante et al. 2008). OCS can also be produced, though at a lower abundance, from irradiation of a mixture of  $\text{CO}_2$ , which dissociates the  $\text{CO}_2$  into CO, and  $\text{H}_2\text{S}$ . We compared OCS with CO abundances for comets when both values were reported in the literature. Since the OCS vacuum sublimation temperature is  $\sim 85$  K (Palumbo et al. 1995; Ferrante et al. 2008), the high volatility and lower thermal threshold of CO makes evolutionary processing effects more important for CO than for OCS. Figure 6 suggests a higher CO abundance may be correlated with a higher OCS abundance; however, the very small number of OCS measurements to date in comets precludes establishing a clear correlation between CO and OCS at this time.

The free sulfur required to produce OCS can also come from the dissociation of sulfur dioxide ( $\text{SO}_2$ ) (Okabe 1978, p. 247; Ferrante et al. 2008). Sulfur atoms can also be oxidized by  $\text{H}_2\text{O}$  molecules, yielding  $\text{SO}_2$  (Moore et al. 2007); sufficient oxidation might completely block OCS formation (see Figure 6 of Ferrante et al. 2008). Thus, the formation of OCS in  $\text{H}_2\text{O}$ -dominated ices might be expected to be smaller, which could be the case in parts of the mid-plane of the protoplanetary disk where comets formed. It is not clear how much of the interstellar sulfur molecules survive during star formation to be incorporated into disks, or whether the sulfur chemistry in such environments is mostly reset.

## 6. Conclusion

OCS is an extremely under-represented species in the current taxonomy of cometary volatiles. In this work, (1) we found



**Table 3**  
OCS Abundance (Relative to H<sub>2</sub>O) in Other Comets

Comet	OCS Abundance (%)
C/1999 H1 (Lee) <sup>a</sup>	<3.6
1P/Halley <sup>b</sup>	<0.8
C/1989 C1 (Austin) <sup>c</sup>	<0.55
Hale-Bopp <sup>d</sup>	0.413 ± 0.077
Hale-Bopp <sup>e</sup>	0.4
Hyakutake <sup>f</sup>	<0.53
Hyakutake <sup>g</sup>	0.21
Hyakutake <sup>h</sup>	0.3
Hyakutake <sup>i</sup>	0.1
Hyakutake <sup>j</sup>	0.2
Lovejoy <sup>k</sup>	0.034 ± 0.006
ISON <sup>l</sup>	0.16 ± 0.04
67P <sup>m</sup>	0.12
67P <sup>n</sup>	0.18
67P <sup>n</sup>	0.017
67P <sup>n</sup>	0.098
2P/Encke <sup>o</sup>	0.06 ± 0.01
C/1993 F2 Shoemaker-Levy <sup>p</sup>	<0.2
C/2009 P1(Garradd) <sup>q</sup>	<0.2
153P/Ikeya-Zhang <sup>r</sup>	<0.2

#### Notes.

- <sup>a</sup> Biver et al. (2000).  
<sup>b</sup> Combes et al. (1988) (at 2.5 $\sigma$ ).  
<sup>c</sup> DiSanti et al. (1992).  
<sup>d</sup> Dello Russo et al. (1998) (near-IR).  
<sup>e</sup> Bockelée-Morvan et al. (2000) (radio).  
<sup>f</sup> Dello Russo et al. (1998) (3 $\sigma$  upper limit on March 24.5).  
<sup>g</sup> Dello Russo et al. (1998) (March 19).  
<sup>h</sup> Dello Russo et al. (1998) (using OH<sup>+</sup> production rate derived by Schleicher et al. 1996; March 19).  
<sup>i</sup> Woodney et al. (1997) (radio).  
<sup>j</sup> Biver et al. (1999) (radio).  
<sup>k</sup> Biver et al. (2015).  
<sup>l</sup> Dello Russo et al. (2016a).  
<sup>m</sup> Bockelée-Morvan et al. (2016).  
<sup>n</sup> Le Roy et al. (2015).  
<sup>o</sup> Roth et al. (2018).  
<sup>p</sup> Bockelée-Morvan et al. (1990).  
<sup>q</sup> Paganini et al. (2012).  
<sup>r</sup> Bockelée-Morvan et al. (2004). The values reported for comets C/1999 H1 Lee and 1P/Halley are not stringent as they are much higher compared to the highest abundances measured in other comets and therefore we have excluded them from Figure 5.

clear detections of OCS and H<sub>2</sub>O in comets T7, ER61, and G–Z, and presented a stringent 3 $\sigma$  upper limit in comet Wirtanen, consistent with the lowest reported value in comets to date (see Figure 5, and Tables 2 and 3). (2) Our work significantly expands the range of OCS abundances, increases the number of OCS measurements in comets, and contributes extensively to establishing a more meaningful statistic for this prebiotically important sulfur-bearing species.

Compared to the mean abundances among comets observed to date (0.126 ± 0.034%; see Figure 5), OCS mixing ratios in comets T7 and Wirtanen are consistent with depleted, while values for G–Z and ER61 are close to the unweighted mean value. The availability of future space-based platforms, such as the James Webb Space Telescope (scheduled to launch in 2021), along with the powerful, recently commissioned facility spectrometer iSHELL at the NASA-IRTF enables for the first

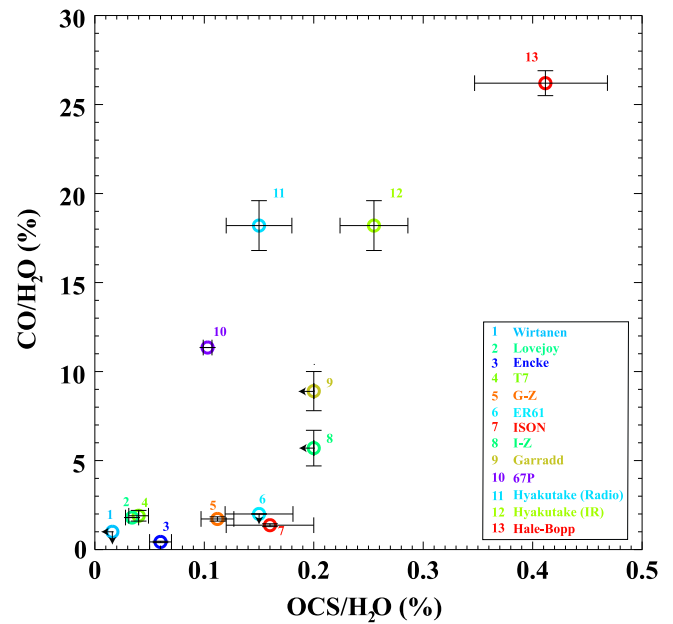


**Figure 6.** Average OCS abundances plotted against average CO abundances (both relative to H<sub>2</sub>O in %). Number and color assigned to each comet are given in the plot legend. The references for OCS abundances are presented in the Figure 5 caption. CO abundances are from: (1) McKay et al. (2019), (2) Biver et al. (2015), (3) Roth et al. (2018), (5) Roth et al. (2020), (6) M. Saki et al. (in preparation), (10) Le Roy et al. (2015), (4, 7, 8, 9, 10, 11, 13) Dello Russo et al. (2016b).

time simultaneously measuring OCS together with H<sub>2</sub>O and CO in comets, further improving our understanding of their chemical diversity.

Data for this study were obtained at the NASA Infrared Telescope Facility (IRTF), operated by the University of Hawaii under contract NNH14CK55B with the National Aeronautics and Space Administration (NASA). We are most fortunate to have the opportunity to conduct observations from Maunakea and recognize and acknowledge the very significant cultural role and reverence that the summit of Maunakea has always had within the indigenous Hawaiian community. We acknowledge the commitment of NASA-IRTF to comet 46P/Wirtanen’s observing campaign in its 2018 historical apparition. This study was generously funded by the NASA Planetary Astronomy/Solar System Observations (NNX12AG24G, 15-SSO15\_2-0028, 18-SSO18\_2-0040), Planetary Atmospheres (NNX12AG60G) and Solar System Workings Programs (NNX17AC86G), the NASA Astrobiology Institute (13-13NAI7\_2\_0032), the NASA Emerging Worlds Program (NNN12AA01C and 80NSSC20K0341), the National Science Foundation (AST-1616306, AST-1615441), NASA Headquarters under the NASA Earth and Space Science Fellowship Program (grant NNX16AP49H). We thank an anonymous reviewer for suggestions that improved the paper. We acknowledge and thank the entire staff at IRTF for their support during our observations.

#### ORCID iDs

Mohammad Saki <https://orcid.org/0000-0003-2277-6232>  
 Erika L. Gibb <https://orcid.org/0000-0003-0142-5265>  
 Boncho P. Bonev <https://orcid.org/0000-0002-6391-4817>  
 Nathan X. Roth <https://orcid.org/0000-0002-6006-9574>  
 Michael A. DiSanti <https://orcid.org/0000-0001-8843-7511>

Ronald J. Vervack, Jr.  <https://orcid.org/0000-0002-8227-9564>  
 Adam J. McKay  <https://orcid.org/0000-0002-0622-2400>  
 Hideyo Kawakita  <https://orcid.org/0000-0003-2011-9159>

## References

- A'Hearn, M. F. 2017, *RSPTA*, **375**, 20160261  
 Anderson, W. M. 2010, PhD thesis, The Catholic Univ. America  
 Biver, N., Bockelée-Morvan, D., Crovisier, J., et al. 1999, *AJ*, **118**, 1850  
 Biver, N., Bockelée-Morvan, D., Crovisier, J., et al. 2006, *A&A*, **449**, 1255  
 Biver, N., Bockelée-Morvan, D., Crovisier, J., et al. 2000, *AJ*, **120**, 1554  
 Biver, N., Bockelée-Morvan, D., Moreno, R., et al. 2015, *SciA*, **1**, e1500863  
 Bockelée-Morvan, D., Crovisier, J., Colom, P., et al. 1990, in Proc. of the 24th ESLAB Symp., Formation of Stars and Planets and the Evolution of the Solar System, ed. B. Battrick (Paris: ESA), 143  
 Bockelée-Morvan, D., Crovisier, J., Erard, S., et al. 2016, *MNRAS*, **462**, S170  
 Bockelée-Morvan, D., Crovisier, J., Mumma, M. J., & Weaver, H. A. 2004, in Comets II, ed. M. C. Festou, H. U. Keller, & H. A. Weaver (Tucson, AZ: Univ. Arizona Press), 391  
 Bockelée-Morvan, D., Lis, D., Wink, J., et al. 2000, *A&A*, **353**, 1101  
 Bonev, B. P. 2005, PhD thesis, Univ. Toledo, [http://astrobiology.gsfc.nasa.gov/Bonev\\_thesis.pdf](http://astrobiology.gsfc.nasa.gov/Bonev_thesis.pdf)  
 Bonev, B. P., Mumma, M. J., Radeva, Y. L., et al. 2008, *ApJL*, **680**, L61  
 Brooke, T. Y., Weaver, H. A., Chin, G., et al. 2003, *Icar*, **166**, 167  
 Calmonte, U., Altwegg, K., Balsiger, H., et al. 2016, *MNRAS*, **462**, 253  
 Cochran, A. L., Lvasseur-Regourd, A.-C., Cordiner, M., et al. 2015, *SSRv*, **197**, 9  
 Combes, M., Crovisier, J., Encrenaz, T., Moroz, V. I., & Bibring, J.-P. 1988, *Icar*, **76**, 404  
 Cordiner, M. A., Remijan, A. J., Boissier, J., et al. 2014, *ApJL*, **792**, L2  
 Dello Russo, N., DiSanti, M. A., Mumma, M. J., Magee-Sauer, K., & Rettig, T. W. 1998, *Icar*, **135**, 377  
 Dello Russo, N., Kawakita, H., Vervack, R. J., Jr., & Weaver, H. A. 2016a, *Icar*, **278**, 301  
 Dello Russo, N., Vervack, R. J., Jr., Kawakita, H., et al. 2016b, *Icar*, **266**, 152  
 DiSanti, M. A., Bonev, B. P., Dello Russo, N., et al. 2017, *AJ*, **154**, 246  
 DiSanti, M. A., Bonev, B. P., Gibb, E. L., et al. 2016, *ApJ*, **820**, 34  
 DiSanti, M. A., Bonev, B. P., Magee-Sauer, K., et al. 2006, *ApJ*, **650**, 470  
 DiSanti, M. A., Mumma, M. J., Dello Russo, N., & Magee-Sauer, K. 2001, *Icar*, **153**, 361  
 DiSanti, M. A., Mumma, M. J., & Lacy, J. H. 1992, *Icar*, **97**, 155  
 DiSanti, M. A., Villanueva, G. L., Paganini, L., et al. 2014, *Icar*, **228**, 167  
 Ehrenfreund, P., Irvine, W., Becker, L., et al. 2002, *RPPH*, **65**, 1427  
 Ferrante, R. F., Moore, M. H., Spiliotis, M. M., & Hudson, R. L. 2008, *ApJ*, **684**, 1210  
 Fuente, A., Cernicharo, J., Agúndez, M., et al. 2010, *A&A*, **524**, A19  
 Geballe, T. R., Baas, F., Greenberg, J. M., & Schutte, W. 1985, *A&A*, **146**, L6  
 Gibb, E. L., Bonev, B. P., Villanueva, G. L., et al. 2012, *ApJ*, **750**, 102  
 Gomes, R., Levison, H. F., Tsiganis, K., & Morbidelli, A. 2005, *Natur*, **435**, 466  
 Greene, T. P., Tokunaga, A. T., Toomey, D. W., & Carr, J. S. 1993, *Proc. SPIE*, **1946**, 313  
 Gronoff, G., Maggioletto, R., Cessateur, G., et al. 2020, *ApJ*, **890**, 89  
 Guilloteau, S., Di Folco, E., Dutrey, A., et al. 2013, *A&A*, **549**, A92  
 Guilloteau, S., Reboussin, L., Dutrey, A., et al. 2016, *A&A*, **592**, A124  
 Hawkins, M., Almond, M. J., & Downs, A. J. 1985, *JPhCh*, **89**, 3326  
 Isoniemi, E., Pettersson, M., Khriachtchev, L., Lundell, J., & Rasanen, M. 1999, *JPCA*, **103**, 696  
 Jiménez-Escobar, A., Muñoz Caro, G. M., & Chen, Y. J. 2014, *MNRAS*, **443**, 343  
 Kamp, L. W., & Taylor, F. W. 1990, *Icar*, **86**, 510  
 Laas, J. C., & Caselli, P. 2019, *A&A*, **624**, A108  
 Le Gal, R., Öberg, K. I., Loomis, R. A., et al. 2019, *AJ*, **876**, 72  
 Leman, L., Orgel, L., & Ghadiri, M. R. 2004, *Sci*, **306**, 283  
 Le Roy, L., Altwegg, K., Balsiger, H., et al. 2015, *A&A*, **583**, A1  
 Levison, H. F., Morbidelli, A., Tsiganis, K., et al. 2011, *AJ*, **142**, 152  
 McKay, A. J., DiSanti, M. A., Bonev, B. P., et al. 2019, EPSC, 2019, EPSC-DPS2019-1061  
 Millar, T. J., & Herbst, E. 1990, *A&A*, **231**, 466  
 Moore, M. H., Hudson, R. L., & Carlson, R. W. 2007, *Icar*, **189**, 409  
 Mumma, M. J., & Charnley, S. B. 2011, *ARA&A*, **49**, 471  
 Nesvorný, D., Vokrouhlický, D., Dones, L., et al. 2017, *API*, **845**, 27  
 Okabe, N. 1978, Photochemistry of Small Molecules (New York: Wiley)  
 Pacheco-Vázquez, S., Fuente, A., Baruteau, C., et al. 2016, *A&A*, **589**, A60  
 Paganini, L., & Mumma, M. J. 2016, *ApJS*, **226**, 3  
 Paganini, L., Mumma, M. J., Gibb, E. L., & Villanueva, G. L. 2017, *ApJL*, **836**, L25  
 Paganini, L., Mumma, M. J., Villanueva, G. L., et al. 2012, *ApJL*, **758**, L13  
 Palumbo, M. E., Geballe, T. R., & Tielens, A. G. G. M. 1997, *ApJ*, **479**, 839  
 Palumbo, M. E., Tielens, A. G. G. M., & Tokunaga, A. T. 1995, *ApJ*, **449**, 674  
 Phuong, N. T., Chapillon, E., Majumdar, L., et al. 2018, *A&A*, **616**, L5  
 Radeva, Y. L., Mumma, M. J., Bonev, B. P., et al. 2010, *Icar*, **206**, 764  
 Rayner, J., Bond, T., Bonnet, M., et al. 2012, *Proc. SPIE*, **8446**, 84462C  
 Rayner, J., Tokunaga, A., Jaffe, D., et al. 2016, *Proc. SPIE*, **9908**, 99088A  
 Rickman, H., Marchi, S., A'Hearn, M. F., et al. 2015, *A&A*, **583**, A44  
 Roth, N. X., Gibb, E. L., Bonev, B. P., et al. 2018, *AJ*, **156**, 251  
 Roth, N. X., Gibb, E. L., Bonev, B. P., et al. 2020, *AJ*, **159**, 42  
 Ruffle, D. P., Hartquist, T. W., Caselli, P., & Williams, D. A. 1999, *MNRAS*, **306**, 691  
 Sakai, N., Oya, Y., López-Sepulcre, A., et al. 2016, *ApJL*, **820**, L34  
 Sakai, N., Sakai, T., Hirota, T., et al. 2014, *Natur*, **507**, 78  
 Schleicher, D., Millis, R., Jorda, L., et al. 1996, *IAUC*, **6344**, 1  
 Stern, S. A. 2003, *Natur*, **424**, 639  
 Teague, R., Henning, T., Guilloteau, S., et al. 2018, *ApJ*, **864**, 133  
 Tiefertunk, A., Pineau des Forets, G., Schilke, P., & Walmsley, C. M. 1994, *A&A*, **289**, 579  
 Tokunaga, A. T., Toomey, D. W., Carr, J., Hall, D. N. B., & Epps, H. W. 1990, *Proc. SPIE*, **1235**, 131  
 Vastel, C., Quénard, D., Le Gal, R., et al. 2018, *MNRAS*, **478**, 5514  
 Vidal, T. H. G., Loison, J.-C., Jaziri, A. Y., et al. 2017, *MNRAS*, **469**, 435  
 Vidal, T. H. G., & Wakelam, V. 2018, *MNRAS*, **474**, 5575  
 Villanueva, G. L., Mumma, M. J., Bonev, B. P., et al. 2009, *ApJL*, **690**, L5  
 Villanueva, G. L., Mumma, M. J., Bonev, B. P., et al. 2012, *JQSRT*, **113**, 202  
 Villanueva, G. L., Mumma, M. J., DiSanti, M. A., et al. 2011, *Icar*, **216**, 227  
 Villanueva, G. L., Mumma, M. J., Novak, R. E., & Hewagama, T. 2008, *Icar*, **195**, 34  
 Villanueva, G. L., Smith, M. D., Protopapa, S., Faggi, S., & Mandell, A. M. 2018, *JQSRT*, **217**, 86  
 Vokrouhlický, D., Nesvorný, D., & Dones, L. 2019, *AJ*, **157**, 81  
 Woodney, L. M., McMullin, J., & A'Hearn, M. F. 1997, *P&SS*, **45**, 717  
 Woods, P. M., Occhiogrosso, A., Viti, S., et al. 2015, *MNRAS*, **450**, 1256  
 Zasowski, G., Kemper, F., Watson, D. M., et al. 2009, *ApJ*, **694**, 459  
 Zolensky, M. E., Zega, T. J., Yano, H., et al. 2006, *Sci*, **314**, 1735